A&A 665, A81 (2022)
https://doi.org/10.1051/0004-6361/202243443

Astronomy & Astrophysics

Does the Fe L-shell blend bias abundance measurements in intermediate-temperature clusters?

Giacomo Riva[1,2], Simona Ghizzardi[1], Silvano Molendi[1], Iacopo Bartalucci[1], Sabrina De Grandi[3], Fabio Gastaldello[1], Claudio Grillo[1,2], and Mariachiara Rossetti[1]

[1] INAF – Istituto di Astrofisica Spaziale e Fisica Cosmica di Milano, Via A. Corti 12, 20133 Milano, Italy
e-mail: giacomo.riva@inaf.it
[2] Dipartimento di Fisica, Universitá degli Studi di Milano, Via G. Celoria 16, 20133 Milano, Italy
[3] INAF – Osservatorio Astronomico di Brera, Via E. Bianchi 46, 23807 Merate, Italy

Received 1 March 2022 / Accepted 22 June 2022

ABSTRACT

In intermediate-mass galaxy clusters ($M = 2{-}4 \times 10^{14}\,M_{\odot}$, or equivalently $T = 2.5{-}4.5$ keV), abundance measurements are almost equally driven by iron K and L transitions at ~6.7 keV and 0.9−1.3 keV, respectively. While K-shell-derived measurements are considered reliable, the resolution of the currently available instrumentation, as well as our current knowledge of the atomic processes, makes the modelling of the L-line complex challenging, resulting in potential biases for abundance measurements. In this work we study with unprecedented accuracy the systematics related to the modelling of the Fe L-line complex that may influence iron-abundance measurements in the intermediate-mass range. To this end, we selected a sample of three bright and nearby galaxy clusters, with long *XMM-Newton* observations available and temperatures in the 2.5−4.5 keV range. We fit the spectra extracted from concentric rings with APEC and APEC+APEC models, by alternately excluding one band (L-shell or Kα) at a time, and derived the fractional difference of the metal abundances $\Delta Z/Z$ as an indication of the consistency between K- and L-shell-derived measurements. The $\Delta Z/Z$ distribution was then studied as a function of the cluster radius, ring temperature, and X-ray flux. The L-blend-induced systematics, measured through an individual fit of each *XMM-Newton* MOS and pn camera spectrum, remain constant at a 5−6% value in the whole 2.5−4.5 keV temperature range. Conversely, a joint fit of MOS and pn spectra leads to a slight excess of 1−2% in this estimate. No significant dependence on the ring X-ray flux is highlighted. The measured 5−8% value indicates a modest contribution of the systematics to the derived iron abundances, giving confidence for future measurements. To date, these findings represent the best achievable estimate of the systematics in analysis, while future microcalorimeters will significantly improve our understanding of the atomic processes underlying the Fe L emissions.

Key words. X-rays: galaxies: clusters – intergalactic medium – galaxies: abundances

1. Introduction

During the last decades, several studies have focussed on the measurement of the metallicity in galaxy clusters and groups (see Mernier et al. 2018; Gastaldello et al. 2021 for a review). Since they are the largest structures to have clearly decoupled from the Hubble flow, studies of metal abundance in the intracluster medium (ICM) provide important clues to the cluster formation and evolution processes, and to the enrichment of the Universe. Since the 1950s, when the first complete theories of stellar nucleosynthesis were developed (Cameron 1957; Burbidge et al. 1957), it has generally been accepted that most of the chemical elements heavier than helium are produced in stars at different stages of their lifetimes, particularly at the end (see Nomoto et al. 2013 for a review). Although the synthesis processes of the heavy elements in the Universe are known fairly well, the general picture of the enrichment history in galaxy clusters and groups is still far from being completely clear.

Galaxy-cluster outskirts have recently enjoyed particular attention since they provide direct information on the ICM (its formation, accretion, and contribution to the growth of large-scale structures; Walker et al. 2019). However, iron-abundance measurements are not easy to perform in clusters, especially in their outermost low surface brightness regions. Reliable measurements have typically been carried out up to $R \sim 0.6\,R_{500}$[1], sampling about one-third of the total gas mass in clusters (as discussed in Molendi et al. 2016) and only on archival samples without guarantee of representativity (Mernier et al. 2017; Leccardi & Molendi 2008a; Lovisari & Reiprich 2019). In this context, a very large programme on *XMM-Newton* (the *XMM-Newton* Cluster Outskirts Project, X-COP; Eckert et al. 2017) has been carried out to advance our knowledge of the physical conditions in the cluster outskirts, pushing the analyses up to R_{500} for a sample of 12 massive galaxy clusters ($M_{500} > 4 \times 10^{14}\,M_{\odot}$) selected from the *Planck* all-sky survey of Sunyaev–Zeldovich (SZ, Sunyaev & Zeldovich 1972) sources (Planck Collaboration XXIX 2014; Planck Collaboration XXVII 2016).

Within this programme, Ghizzardi et al. (2021a) derived for the first time robust metallicity profiles up to R_{500} for a sample of galaxy clusters, and identified the main systematic error that affects iron-abundance measurements in the cluster outskirts. In the central regions of massive clusters (such as the X-COP

[1] R_{Δ} is the radius inside which the cluster mass density is Δ times the critical density of the Universe $\rho_c(z) = 3H_0^2E(z)^2/8\pi G$, where $E(z) = \sqrt{\Omega_m(1+z)^3+\Omega_{\Lambda}}$ (in a flat Universe) and z is the redshift; M_{Δ} is then defined as the total mass within R_{Δ}.

sample, where temperatures are higher than 4 keV) iron-abundance measurements are mostly driven by the Fe K transitions (mainly by Fe XXV and Fe XXVI Kα lines) at ~6.7 keV in the ICM spectrum, while the equivalent width (EW) of the Fe L-line complex (0.9−1.3 keV) is smaller (see Fig. 3 of their work). Hereafter we refer to these transitions simply as Kα and L-shell, respectively. However, going towards the cluster outskirts, the EW of the Kα decreases with respect to the total continuum, which is dominated by the background emission, and the L-shell assumes a primary role in the fit (see Fig. 4 of their work). The L-line-derived abundance measurements in such a high-background regime were found to be extremely puzzling in some cases, making the reliability of the L-shell in abundance measurements questionable. The exclusion of the L-shell (0.9−1.3 keV) energy band was found to lead to more reliable abundance profiles, which renewed some old but still relevant questions, for example whether the L-shell-derived abundance measurements are unreliable in general or if they become so only in specific and complex situations.

At the spectral resolution of currently available CCD cameras the single lines that build up the L-shell (see Hwang et al. 1997; Mazzotta et al. 1998; Gu et al. 2019, 2020; Heuer et al. 2021) are not resolved and are actually seen as a blend (see Fig. 1 in Gastaldello & Molendi 2002). The large number of Fe emission lines peaking in the 0.9−1.3 keV energy range and our current knowledge of the atomic processes make the modelling of the L-shell challenging, resulting in potential biases. Conversely, the Fe Kα at ~6.7 keV is relatively well understood, especially after the data release of the SXS spectrum of Perseus (Aharonian 2018). In the late 1990s Hwang et al. (1997) quantified possible L-shell-induced systematics by comparing Kα- and L-blend-derived iron abundances for a few galaxy clusters (with ASCA observations) in the 2−4 keV temperature range. Their research did not highlight any significant discrepancies between the K- and L-derived measurements within the 90% confidence level. However, the large error bars of their results do not allow a precise assessment of the reliability of the L-shell-derived abundance measurements.

Currently, we can rely on satellites with advanced characteristics (e.g. the large effective area of *XMM-Newton*) and also on atomic codes (e.g. AtomDB[2], implemented in the APEC model as part of the XSPEC[3] fitting package; Smith et al. 2001; Foster et al. 2012; SPEXACT, available in the SPEX[4] fitting package; Kaastra et al. 1996, 2018), which describe the atomic processes that produce the emission lines observed in the ICM spectra with greater precision than in the past. These instruments allow us to study with high accuracy the systematics related to the L-shell that affect iron-abundance measurements. In this work we compare Kα- and L-shell-derived abundance measurements for a sample of galaxy clusters observed with *XMM-Newton* and with temperatures in the 2.5−4.5 keV range. In this range the EWs of the L-shell (at these temperatures primarily due to Fe XXIII and XXIV) and Kα emissions are comparable, giving us the possibility to test the atomic codes underlying abundance measurements.

The paper is organised as follows. In Sect. 2 we present our sample and the data reduction. Section 3 is dedicated to the X-ray data analysis; here we define the strategies used to estimate the L-shell-induced systematics. In Sect. 4 we analyse a possible dependence of the systematics on the temperature and the flux. Section 5 is dedicated to the discussion of the results. Finally, we summarise our main findings in Sect. 6.

Throughout the paper, we assume a Λ cold dark matter (CDM) cosmology with $H_0 = 70\,\mathrm{km\,s^{-1}\,Mpc^{-1}}$, $\Omega_\mathrm{m} = 0.3$, $\Omega_\Lambda = 0.7$, and $E(z) = \sqrt{\Omega_\mathrm{m}(1+z)^3 + \Omega_\Lambda}$ for the evolution of the Hubble parameter. The solar abundance table is set to Asplund et al. (2009), while all the quoted errors hereafter are at the 1σ confidence level.

2. Selection of the sample and data processing

In this work we restrict our analysis to a sample of nearby and bright clusters with (i) long *XMM-Newton* observations ($\gtrsim$120 ks), (ii) good statistics, (iii) regions with temperature in the 2.5−4.5 keV range, and (iv) high source-to-background (S/B) ratios. Our aim is to focus on the contribution to the systematics related to the underlying atomic model in the above temperature range, studying cluster regions where contributions from the background contamination can be neglected. To this end, we select the following galaxy clusters: Perseus, 2A 0335+096, and Sérsic 159−03 (Table 1).

For each cluster, we only consider the longest available observation in the *XMM-Newton* Science Archive (XSA), to avoid additional systematics deriving from a combination of different observations of the same cluster. The identification numbers of the selected observations are listed in Table 1, together with the cluster redshifts, temperatures, and X-ray fluxes in the 0.1−2.4 keV band. Given the redshifts of the three clusters (see Table 1), $1'$ corresponds to 22 kpc, 43 kpc, and 65 kpc for Perseus, 2A 0335+096, and Sérsic 159−03, respectively.

The X-ray data are reduced using the *XMM-Newton* Science Analysis Software (SAS). The main steps of the data processing are the following. First, we start by producing calibrated event files for each observation (with *emchain* and *epchain* tasks). Second, we extract light curves in the hard band (10−12 keV for the MOS detectors and 10−13 keV for pn) by using 100 s binning. We filter out time intervals affected by soft-proton flares by applying the appropriate threshold for each instrument. For the MOS detectors we adopt a threshold of 0.25, 0.17, and 0.16 cts s^{-1} for Perseus, 2A 0335+096, and Sérsic 159−03, respectively, while the threshold is set to 0.70, 0.43, and 0.42 cts s^{-1} for the three pn light curves. Third, following Leccardi & Molendi (2008b), we then reject the time periods in which the count rates exceed 3σ from the median of the light curve in the 2−5 keV band in order to eliminate the contributions of softer flares. The effective exposure times of the MOS and pn cameras after the soft-proton cleaning are listed in Table 1. Finally, we select by eye and excise the bright point sources inside the regions from which spectra are extracted (see next section).

A characterisation of the local sky background cannot be considered for Perseus, 2A 0335+096, and Sérsic 159−03 since their thermal emissions fill the whole *XMM-Newton* field of view. For this reason, and since we are interested in studying the L-shell systematics in conditions of relatively high surface brightness where the background subtraction is less critical than for external low surface brightness regions, we used blank-sky fields instead of proceeding with a more detailed modelling of the different background components. In Sect. 4.1 we investigate the impact of this choice on our results. The blank-sky fields for the EPIC MOS and pn were produced by Leccardi & Molendi (2008b). We performed a background rescaling for each observation to account for temporal variations of the background (Leccardi & Molendi 2008b; Ghizzardi et al. 2014).

[2] http://www.atomdb.org
[3] https://heasarc.gsfc.nasa.gov/xanadu/xspec
[4] https://www.sron.nl/astrophysics-spex

Table 1. Cluster properties and information of the *XMM-Newton* observations.

Cluster	Obs. ID	MOS exposure (ks)	pn exposure (ks)	R_{500} (Mpc)	T (keV)	Flux (0.1−2.4 keV) (erg s^{-1} cm^{-2})	z
Perseus	0305780101	118	94	1.3	3.5−4.5	9.61×10^{-10}	0.018
2A 0335+096	0147800201	79	76	0.9	2.4−3.5	9.16×10^{-11}	0.036
Sérsic 159−03	0147800101	86	77	0.8	2.5−2.7	2.49×10^{-11}	0.056

Notes. 'MOS Exposure' and 'pn Exposure' are the effective exposure times of the MOS and pn cameras after the soft-proton cleaning. Estimates for R_{500} are taken from Giacintucci et al. (2019) for Perseus and 2A 0335+096, and from Sun et al. (2009) for Sérsic 159−03. Listed for each cluster are the temperature ranges covered by the various regions for which we extracted and fitted the spectra. These temperatures are in the ranges of interest. Regions with temperatures higher than 4.5 keV are not considered for Perseus, as explained in Sect. 3.2.1. The Perseus flux and redshift are from Ebeling et al. (2002); for 2A 0335+096 and Sérsic 159−03, we refer to de Plaa et al. (2007) and Sanders et al. (2011) for the flux and the redshift, respectively.

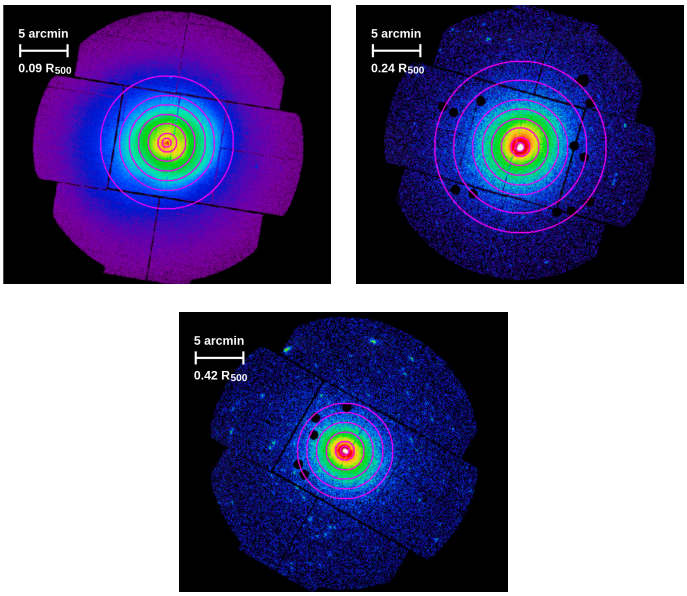

Fig. 1. Surface brightness map (MOS 2 camera) of Perseus (*top left*), 2A 0335+096 (*top right*), and Sérsic 159−03 (*bottom*), extracted in the 0.15−12 keV band. X-ray point sources selected during the data reduction are excised. The rings from which the X-ray spectra are extracted are shown in magenta. Given the redshifts of the three clusters (see Table 1), 1′ corresponds respectively to 22 kpc, 43 kpc, and 65 kpc for Perseus, 2A 0335+096, and Sérsic 159−03.

3. Data analysis

3.1. Spectral fitting

We extracted spectra from concentric rings (with the centre located at the X-ray emission peak) to derive radial abundance profiles for each cluster. Spectra are extracted up to 7′, 9′, and 5′ for Perseus, 2A 0335+096, and Sérsic 159−03, respectively (Fig. 1), according to the following pattern: rings are (i) 0.5′ wide within 1′, (ii) 1′ wide up to 5′, and (iii) 2′ wide at larger radii. Given the statistics of the three selected clusters, the above ring angular dimensions allow temperature and abundance radial profiles to be derived with good precision. As detailed below, the external limit for Perseus is set by the high temperature at large radii, while in the case of 2A 0335+096 and Sérsic 159−03 we are limited by the presence of an increasingly dominating background.

Spectra are fitted using XSPEC v.12.9.1p (Arnaud 1996). At first, the MOS and pn spectra of each region are fitted separately. We then perform a joint fit of the three cameras. The spectra are grouped to ensure a minimum of 25 counts per spectral channel. Unless otherwise stated, the energy range considered in the fitting is 0.7−10 keV. We adopted two models: an absorbed (phabs) single-temperature APEC model (hereafter 1T model), with temperature, Galactic hydrogen column density $N_{\rm H}$, abundance, redshift, and normalisation free to vary, and an absorbed (phabs) double-temperature APEC+APEC model, with two abundances linked together (hereafter 2T model). In this case, temperatures, Galactic hydrogen column density, abundance, redshift, and normalisations are also free to vary.

As further addressed in Sect. 3.2.2, the single-temperature 1T model is adequate for cluster rings that can be considered nearly isothermal, while the double-temperature 2T model better describes the data in case of multiphase plasma. The 2T model is also useful for mimicking and describing cases where multiphaseness is artificial and due to projection or to contamination from adjacent rings. For this reason we do not correct data for point spread function or deproject profiles and use the 2T model to take into account these effects.

3.2. Estimate of the systematic error

The estimation of the systematic error associated with the Fe L-shell follows three major steps, which will be addressed in the following subsections. First, we exclude cluster rings whose properties are not adequate for our purpose. Second, we select the model that best describes the data for each spectrum. Third, we define the strategies for the estimate of the systematics.

3.2.1. Selection of the rings

As already discussed, the aim of this work is the study of systematics related to the L-shell at intermediate temperatures (T = 2.5−4.5 keV) and in conditions of negligible background contamination. For this reason, starting from the general ring selection defined at the beginning of Sect. 3.1, we make the following considerations.

The innermost central bin (0′−0.′5) is not considered for any cluster. Projection effects play a significant role in the central regions, particularly in the innermost bin where the temperature gradient becomes very steep; here neither the 1T nor the 2T model adequately describes the spectra in this circumstance. Since our focus is the study of L-shell-induced systematics rather than modelling the temperature distribution in such a central region, for each cluster we reject the central bin from the analysis. Moreover, Perseus and Sérsic 159−03 are experiencing a phase of AGN feedback in their cores (Gendron-Marsolais et al. 2016; Werner et al. 2011; Farage et al. 2012), which dominates the X-ray emission in the innermost region.

Radial bins whose temperature exceeds the range of interest are excluded from the analysis. This requirement places limits only on Perseus, whose temperature exceeds 5 keV beyond 3′. Radial bins where the background emission is comparable to the source emission in the Kα region (~6.7 keV) are also excluded from the analysis. This choice places limits on 2A 0335+096 and Sérsic 159−03, where radii larger than 5′ and 3′, respectively, are not considered.

After the above considerations, we focus on the spectra extracted from the following rings:
- 0.′5−1′, 1′−2′, 2′−3′ for Perseus;
- 0.′5−1′, 1′−2′, 2′−3′, 3′−4′, 4′−5′ for 2A 0335+096;
- 0.′5−1′, 1′−2′, 2′−3′ for Sérsic 159−031.

3.2.2. Selection of the model

In order to select the model that provides the best description of the data for each spectrum, we fit all the spectra with both the 1T and the 2T models. As a first step we qualitatively analyse how the residuals (i.e. the ratio of the data to the model) vary, using the two models at high energy (beyond 5 keV) and around the L-shell and the Kα energy bands. The presence of an excess in the residuals at high energy, as well as a tension between the residuals around the L-shell and the Kα, is a clear indication that a double-temperature model is needed in the fitting. This qualitative inspection allows us to assess that the 2T model is required at small radii ($r < 3'$, <2′, and <2′ for Perseus, 2A 0335+096, and Sérsic 159−03, respectively), while the 1T model correctly describes 2A 0335+096 and Sérsic 159−03 data at external radii.

In order to quantitatively support our preliminary inferences, we compare the χ^2/d.o.f. values obtained for each fit. This comparison confirms that, for inner radii, the double-temperature model is needed, while for external radii the clusters in our sample can be considered nearly isothermal.

3.2.3. Estimate of the systematics

To estimate the systematic error related to the L-shell, we follow two slightly different strategies. We fit each spectrum with the selected model (1T or 2T, see previous section), alternately excluding the L-shell (0.9−1.3 keV) and the Kα bands (6.3−6.9 keV, 6.2−6.8 keV, and 6.1−6.7 keV[5] for Perseus, 2A 0335+096, and Sérsic 159−03, respectively). In strategy 1 the temperatures are free to vary in this operation. In strategy 2 the temperatures are frozen to the best-fit values derived by fitting over the whole 0.7−10 keV energy range.

In this way, the iron abundance can be measured through the L-shell and the Kα emissions separately, providing an estimate of the difference between the two. Since the physics underlying the Kα emission is simpler and better understood than that for the L-shell blend (as discussed in the Sect. 1), we attribute the above difference to a systematic error in the L-shell measurement. This error is quantified as

$$\frac{\Delta Z}{Z} = \frac{Z_{\text{L-shell}} - Z_{\text{K}\alpha}}{Z_{\text{K}\alpha}}, \quad (1)$$

where $Z_{\text{L-shell}}$ and $Z_{\text{K}\alpha}$ are the iron abundances measured after excluding the Kα and the L-shell energy bands, respectively. Here $Z_{\text{K}\alpha}$ is considered a reference in the iron-abundance measurement. The values obtained for $Z_{\text{K}\alpha}$ and $Z_{\text{L-shell}}$ for each cluster and for the two strategies are listed in Appendix A.

[5] The Kα energy band slightly changes with the cluster redshift.

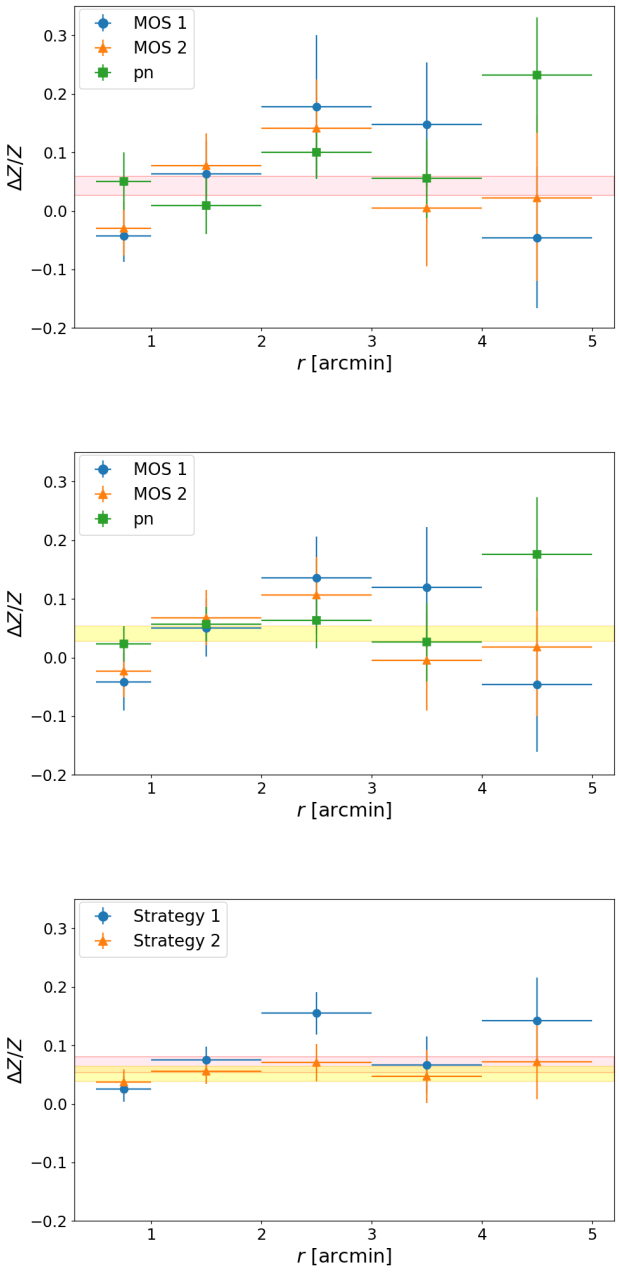

Fig. 2. Radial profile of the systematic error $\Delta Z/Z$ for 2A 0335+096. *Top* and *middle panels*: results obtained through an individual fit of the MOS and pn spectra of each region are shown, following strategy 1 and 2, respectively. *Bottom panel*: same profiles are shown, with the MOS and pn spectra of each region considered jointly in the fitting. The weighted averages of the results are shown, together with their 1σ errors, as the pink and the yellow regions for strategy 1 and 2, respectively.

The two strategies are applied to each cluster in the sample and the systematics are studied as a function of the cluster radii. As an example, in Fig. 2 (top and centre) we show the results obtained for 2A 0335+096 following strategies 1 and 2 and by separately fitting MOS and pn spectra; the values obtained through a joint fit of the three detector spectra are displayed in Fig. 2 (bottom). Figure 2 shows that the systematic error $\Delta Z/Z$ related to the L-shell does not significantly vary with the cluster radius and can be considered constant, both looking at the individual and the joint fits of the MOS and pn spectra. In bright galaxy clusters, where statistical errors become tiny, the

abundances measured by individually fitting MOS and pn data are usually found to be significantly different, due to the well-known cross-calibration issues of the three *XMM-Newton* detectors (Read et al. 2014). Interestingly, however, the MOS and pn cameras lead to $\Delta Z/Z$ values consistent with each other, within the statistical errors, as shown in Fig. 2. The results obtained for Perseus and Sérsic 159−03 are quite similar, and are displayed in Appendix B.

The weighted averages of the results obtained with the individual and with the joint fits for each cluster are shown in Table 2. The average values derived considering the three detectors together are indicated as 'EPIC', while those derived separately are indicated as 'MOS 1', 'MOS 2', and 'pn'. The EPIC averages for 2A 0335+096, obtained through strategies 1 and 2 with both the individual and the joint fits, with the corresponding 1σ errors, are also shown in Fig. 2.

Looking at the values listed in Table 2, we note that the weighted averages of $\Delta Z/Z$ suggest a slightly increasing trend from Sérsic 159−03 to Perseus. However, the large error bars do not allow us to make further considerations and the systematic error estimated for each cluster is consistent with being constant at the same value (∼5−6% and ∼6−8% for the individual and the joint fits, respectively). The joint fits are found to lead to a slight excess of ∼1−2% in the estimate of the systematics associated with the L-shell, with respect to the results obtained with the detectors considered separately. This excess is likely related to the above-mentioned cross-calibration issues of the three *XMM-Newton* detectors (Read et al. 2014), resulting in an additional systematic error.

4. Dependence on temperature and flux

4.1. Systematics vs temperature

The analysis, independently run on the three clusters in our sample, has shown that the systematics related to the L-shell remain constant, both considering different radii of the same cluster (see Fig. 2) and the three clusters themselves (see Table 2). Since each cluster ring has its own temperature, the above result also gives us an indication that systematics seem not to vary with the temperature in the considered range and to be constant with a value of $\Delta Z/Z \sim 5-6\%$ (or at least not higher than 8%). In order to study the dependence, if any, of the systematic error $\Delta Z/Z$ on the temperature, we use the weighted average of $\Delta Z/Z$ (averaged over the three detectors) for each cluster ring. The values obtained are plotted in Fig. 3 (top left and right for strategy 1 and 2, respectively), as a function of the ring temperatures. The temperatures considered in this part of the analysis are obtained for each ring through the 1T model, with independent fits for each *XMM-Newton* camera spectrum, and then averaged over the three detectors[6]. An alternative way of calculating the temperatures for the rings needing the 2T model is to consider a weighted-averaged temperature on the normalisations of the APEC+APEC model. This alternative way does not significantly modify the measured temperatures.

The three clusters in our sample allow us to homogeneously study the 2.5−4.5 keV range. Perseus gives information about the highest temperatures (i.e. the 3.5−4.5 keV range), 2A 0335+096 allows us to study the intermediate 3.0−3.5 keV range, and Sérsic 159−03 (together with the innermost ring for 2A 0335+096) gives an estimate of the systematic error $\Delta Z/Z$ at lower temperatures. Figure 3 (top panels) shows that the systematic error $\Delta Z/Z$ associated with the L-shell remains constant over the studied temperature range. The average values of the results (also reported, together with their 1σ error bars, in Fig. 3, top panels) for strategy 1 and 2, respectively, are the following: $\Delta Z/Z = 0.060 \pm 0.006$; $\Delta Z/Z = 0.049 \pm 0.005$.

Considering MOS and pn spectra separately in the fitting leads to a ∼5−6% systematic error associated with the Fe L-shell in the whole 2.5−4.5 keV temperature range. The result obtained through strategy 2 is slightly lower than that derived through strategy 1, and they are consistent with each other within the error bars. This finding suggests that temperatures free to vary do not significantly affect our results and seem not to introduce additional systematics in the iron-abundance measurements.

We then repeat the same estimate, this time considering a joint fit of the three camera spectra. The results are shown in Fig. 3 (bottom left and right for strategy 1 and 2, respectively). The $\Delta Z/Z$ values estimated through the joint fit also remain constant over the studied temperature range, with the values of $\Delta Z/Z = 0.078 \pm 0.006$ and $\Delta Z/Z = 0.060 \pm 0.005$ for strategy 1 and 2, respectively. As already pointed out, a joint fit of the MOS and pn spectra leads to a ∼1−2% excess in the estimate of the systematic error associated with the L-shell, with respect to an individual fit of each spectrum. We already suggested that this behaviour is likely to be related to a cross-calibration issue of the three detectors (Read et al. 2014), leading to an overestimate of the systematics we are interested in.

Although our study is mainly focussed on bright cluster regions where the background contribution to the total emission is negligible, two of the considered rings (one for 2A 0335+096 and one for Sérsic 159−03; red circles in Fig. 3) also allow us to explore regions where the background emission starts to play a role in the Kα region (S/B ∼ 5 and ∼3 for the most external ring of 2A 0335+096 and Sérsic 159−03, respectively, in the 6−7 keV range). Interestingly, as we see in Fig. 3, the systematics measured for these rings are in agreement, within their 1σ errors, with the average values. This finding suggests that a moderate contamination by the background emission seems not to lead to additional contributions to the systematics we are interested in.

At this point, one may wonder if using blank sky fields instead of a detailed description of each background component leads to significantly biased results, especially for the most external rings of 2A 0335+096 and Sérsic 159−03 where the S/B ratio is smaller. To investigate further this issue, we refit spectra assuming a possible over- and underestimation of the background of 10% in order to evaluate the potential systematics introduced by an incorrect estimate of the background contribution[7]. The $\Delta Z/Z$ values measured after modifying the background emission (and through strategy 2; top right panel of Fig. 3) show little scatter (±1% and ±3% for the most external rings of Sérsic 159−03 and 2A 0335+096, respectively, well below the ±9% and ±7% statistical uncertainties), with respect to the standard (non-modified) value. It should be noted that these tiny variations represent an upper limit to background-related effects on our results, since the central rings are less sensitive to moderate variations in the background contamination, given their significantly higher S/B ratio. These considerations show that the way we treated the background emission does not significantly influence our results and is sufficient for our purpose.

[6] The gap between the temperatures measured for bins 4 and 5 of 2A 0335+096 has been slightly widened, to avoid an overlap of the results.

[7] A 10% variation of the background contribution is above the current uncertainties related to the blank sky fields, which are considered to be about 5%. However, this is useful to place strong limits on background-related systematics.

Table 2. Weighted-averaged $\Delta Z/Z$ values, estimated for Perseus, 2A 0335+096, and Sérsic 159−03.

Cluster	Detector	Individual fit		Joint fit	
		Strategy 1	Strategy 2	Strategy 1	Strategy 2
Perseus	MOS 1	0.056 ± 0.011	0.027 ± 0.011	–	–
	MOS 2	0.044 ± 0.016	0.048 ± 0.012	–	–
	pn	0.076 ± 0.009	0.073 ± 0.010	–	–
	EPIC	0.064 ± 0.007	0.051 ± 0.006	0.081 ± 0.006	0.062 ± 0.006
2A 0335+096	MOS 1	0.020 ± 0.031	0.033 ± 0.029	–	–
	MOS 2	0.030 ± 0.030	0.032 ± 0.027	–	–
	pn	0.067 ± 0.025	0.048 ± 0.018	–	–
	EPIC	0.043 ± 0.016	0.041 ± 0.013	0.068 ± 0.014	0.052 ± 0.013
Sérsic 159−03	MOS 1	−0.033 ± 0.070	−0.031 ± 0.063	–	–
	MOS 2	0.112 ± 0.066	0.128 ± 0.065	–	–
	pn	−0.020 ± 0.046	0.039 ± 0.043	–	–
	EPIC	0.010 ± 0.033	0.042 ± 0.031	0.042 ± 0.032	0.048 ± 0.029

Notes. $\Delta Z/Z$ values are obtained both considering the three *XMM-Newton* cameras independently (indicated with 'MOS 1', 'MOS 2', and 'pn') and together ('EPIC') in the average (see text).

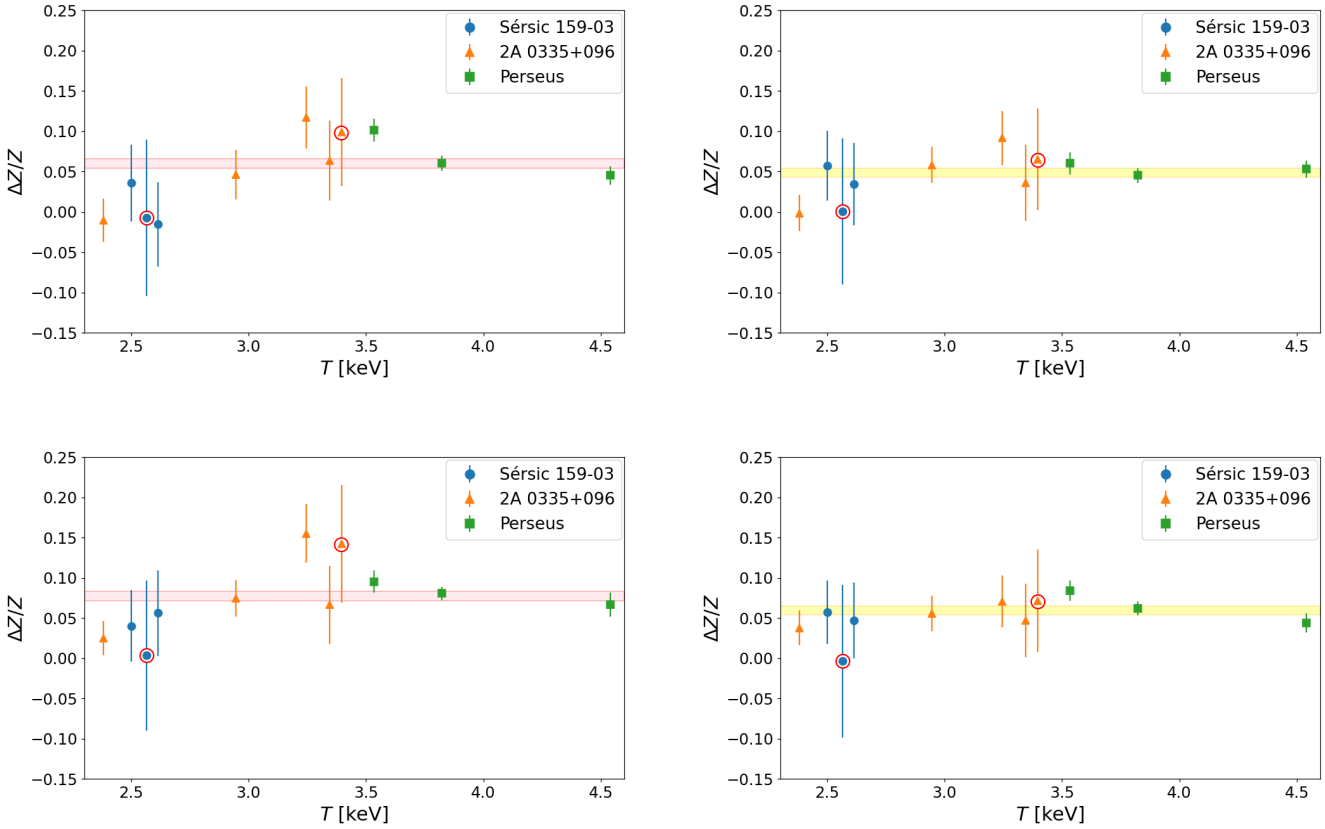

Fig. 3. Systematic error $\Delta Z/Z$ associated with the L-shell as a function of the temperature. *Top* and *bottom rows*: different fitting options (individual and joint fit of the MOS and pn spectra of each region, respectively), *left* and *right column*: refers to strategy 1 and 2, respectively. The pink and the yellow regions represent the weighted averages of the results, together with their 1σ errors.

However, in order to reliably estimate the systematics associated with the L-shell in conditions with stronger background emission, a precise description of the different background components should be considered.

4.2. Systematics vs. flux

We also study a possible dependence of the $\Delta Z/Z$ values on the X-ray flux. In conditions of high source count rates, additional systematic errors may be included in the analysis (e.g. systematics associated with the modelling, calibration issues of the instruments; see Mernier et al. 2018 for a review of the systematic errors that may affect the ICM abundances) and can lead to an overestimate of the systematics related to the L-shell. The X-ray flux of each ring is calculated through the XSPEC *flux* command in the 0.7−10 keV energy range (the same used in the spectral fitting) for the pn camera spectra. The dependence of the systematics on the X-ray flux is shown in Fig. 4. As already discussed for

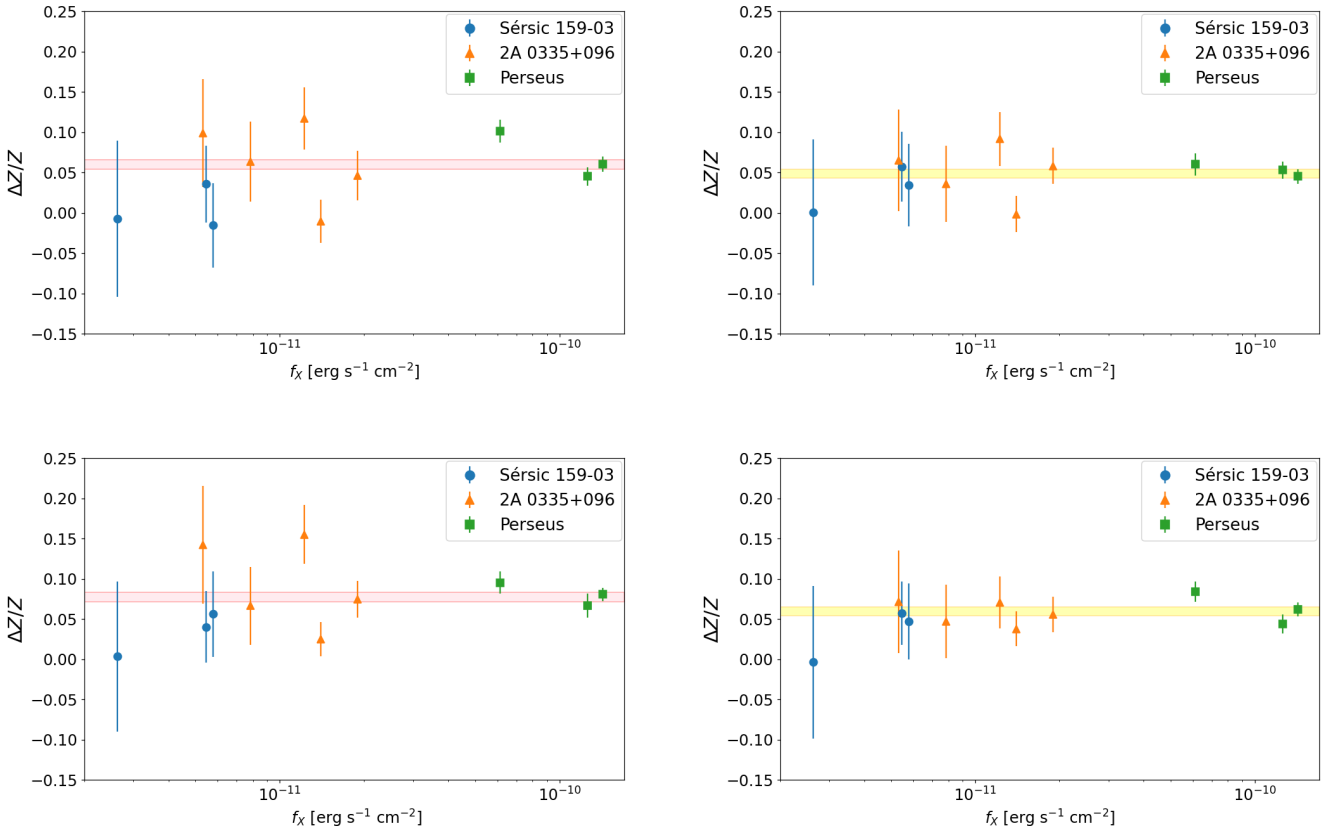

Fig. 4. Systematic error $\Delta Z/Z$ associated with the L-shell as a function of the X-ray flux. The division in the four panels is the same as in Fig. 3. The pink and the yellow regions represent the weighted averages of the results, together with their 1σ errors.

Fig. 3, the left and right panels of Fig. 4 were obtained through strategies 1 and 2, while the top and bottom division refers to the different fitting options of the spectra (individual and joint fit of the MOS and pn spectra of each region, respectively). In Fig. 4 we also show the average $\Delta Z/Z$ values, already discussed in Sect. 4.1.

Figure 4 shows no evident variations with the flux, and the systematic error is consistent with being constant, within the statistical errors, over the considered flux range. In the low-flux range, large statistical errors do not allow us to draw precise conclusions, while at higher flux statistical errors are tiny and the systematics becomes dominant.

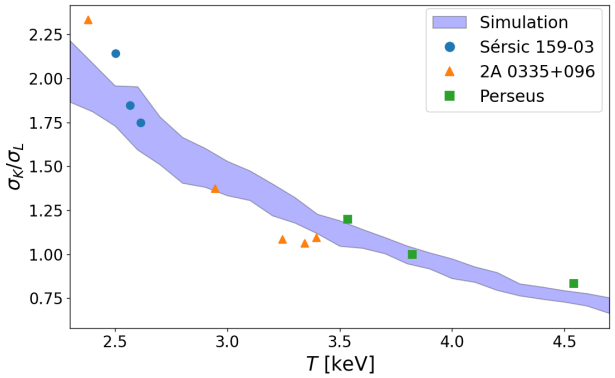

Fig. 5. Ratio of the statistical errors associated with the Kα- and L-shell-derived measurements, as a function of the ring temperatures, for the three clusters in our sample. The violet area represents σ_K/σ_L values (with their 1σ scatter) derived through high-S/B simulated spectra, as explained in the text. The errors are estimated following strategy 2 and through the joint fit of MOS and pn camera spectra of each region. For temperatures lower than ~3.5 keV, the above ratio is higher than 1, meaning that the L-shell drives the abundance measurements.

5. Discussion

In this work we investigate the systematic errors related to the Fe L-shell blend (0.9–1.3 keV energy range), which may affect iron-abundance measurements in intermediate-mass galaxy clusters ($M_{500} = 2\text{–}4\times10^{14}\ M_\odot$, with temperature $T = 2.5\text{–}4.5$ keV). The resolution of the currently available instrumentation, as well as our knowledge of the atomic processes, makes the modelling of the Fe L-shell particularly challenging, resulting in potential biases for our iron-abundance measurements. As already mentioned in the Introduction, at temperatures higher than ~4 keV, iron-abundance measurements are mostly driven by the Kα emission at ~6.7 keV, while in the intermediate 2.5–4.5 keV temperature range, the EW of the Kα line reduces and the L-shell starts to assume a leading role in the fitting.

The increasing importance of the L-shell blend in the fitting is highlighted in Fig. 5, where we show the ratio between the statistical errors associated with $Z_{K\alpha}$ and $Z_{\text{L-shell}}$ (Sect. 3.2.3) for the clusters in our sample, obtained through strategy 2 (Sect. 3.2.3) and with a joint fit of the MOS and pn spectra of each region.

To further highlight the interplay between the Kα and the L-shell emissions at different temperatures, we also produced high-S/B simulated spectra, characterised by single temperature, fixed metallicity ($Z = 0.4\,Z_\odot$), and normalisation equal to 0.1 (the same as for Perseus, one of the brightest clusters of the X-ray sky). We sampled the 2.3–4.7 keV range every 0.1 keV, and

for each step we produced 100 mock spectra with that temperature. By doing this, we were able to measure the median value of the simulated σ_K/σ_L ratio (together with its 1σ uncertainty; violet region in Fig. 5) for each temperature, through strategy 2 and with a joint fit of MOS and pn spectra of each region. Figure 5 shows that our simulation manages to reproduce the measured σ_K/σ_L trend. We found, at temperatures lower than ∼3.5 keV, that the σ_K/σ_L ratio becomes higher than 1, meaning that the L-shell blend has larger statistics than the Kα and represents the leading line emission for the iron-abundance measurement.

The three clusters in our sample (Table 1) allow us to homogeneously study the intermediate 2.5−4.5 keV range (Fig. 3), particularly in conditions of negligible background emission, and thus to explore a temperature range where the transition between the Kα- and L-shell-driven fits is observed. In such a favourable situation, where the Kα and the L-shell emissions have similar EWs, to estimate the systematics associated with the modelling of the L-shell, we can simply compare the L- to the K-derived iron-abundance measurements since the latter are currently considered reliable, as previously discussed. In the case of an individual fit of each detector spectrum, the L-shell is found to lead to ∼5−6% systematics (Fig. 3, top) in the whole 2.5−4.5 keV temperature range. We note that this is actually an upper limit to the systematic error associated with the modelling of the L-shell since this value may include the contribution of other systematics. Conversely, the joint fits of the three detectors lead to ∼6−8% systematics (Fig. 3, bottom), a ∼1−2% excess that is likely due to the cross-calibration issues of the EPIC detectors, as already discussed in Sects. 3.2.3 and 4.1. The strategies we describe in Sect. 3.2.3 represent the most straightforward way to quantify the L-blend-induced systematics and, thanks to a carefully selected sample of galaxy clusters, they lead us to the most accurate (and precise) results that can be obtained with the currently available instrumentation. In this work we carefully focus on a sample of clusters with long *XMM-Newton* observations and high flux in the 0.1−2.4 keV band (Table 1), at low redshifts ($z \sim 0.018-0.056$), and in the 2.5−4.5 keV temperature range. As already discussed, these conditions allowed us to easily compare Kα- and L-shell-derived measurements.

When performing abundance measurements on galaxy clusters, both the Kα and L-shell emission bands are generally used in the fitting to maximise the available statistics. Thus, the measured 5−8% value must be considered an upper limit to the contribution of the L-shell-induced systematics to the derived iron abundances. This consideration gives us confidence for future measurements in intermediate-mass galaxy clusters ($M_{500} = 2-4\times10^{14}\,M_\odot$), at least in low-background-emission regions. In addition, when studying individual galaxy clusters, the precision of the results is usually limited by the poor data quality, where the statistical errors associated with the measured abundances are larger than the derived 5−8% systematics. This means that abundance measurements are usually mostly influenced by the low statistics, while the systematics do not significantly affect the results, making the abundance measurements reliable. However, systematic errors will be dominant when averaging abundance measurements over a sufficiently large sample of clusters. For this reason, when performing iron-abundance measurements over a large sample of intermediate-mass clusters with temperatures lower than ∼3.5 keV, where the L-shell becomes the leading emission, the L-shell-induced systematics should no longer be neglected.

A detailed analysis of the L-shell systematics is of primary importance for future iron-abundance measurements in galaxy-cluster outskirts. As mentioned above, cluster external regions provide important clues to the physical properties of the ICM, and so they have recently enjoyed particular attention. Ghizzardi et al. (2021a,b) focus on the outskirts of massive clusters, but no reliable measurements have been carried out in the intermediate mass (and temperature) range to date. These temperatures, together with the increasing background contribution which occurs in the cluster outskirts, make the L-shell the leading emission for iron-abundance measurements. For this reason an accurate characterisation of the systematics related to the L-shell is required before proceeding with future iron-abundance measurements. In the cluster outskirts, additional systematics (particularly related to the background emission) may influence the measured abundances. However, our work places a limit on the L-shell-induced systematics and is a good starting point for future iron-abundance measurements.

Future X-ray missions, such as XRISM (Tashiro et al. 2018; Guainazzi & Tashiro 2018) and ATHENA (Barret et al. 2013; Cucchetti et al. 2019), will carry microcalorimeters, and this will allow high-resolution spectroscopy to be performed, in turn giving the opportunity to test with unprecedented detail the atomic codes underlying the iron-abundance measurements. Systematic errors related to the spectral resolution of the instrumentation will be less important, while those related to the theoretical models which describe the emission lines will become dominant.

6. Summary

We estimated a systematic error related to the modelling of the Fe L-shell that affects iron-abundance measurements in the 2.5−4.5 keV temperature range. The main results of our work are the following:

- The analysis carried out on three clusters shows that L-shell-induced systematics are in the range 5−8%, depending on the strategy and on the spectral fitting option (Fig. 2). This result indicates that systematics have a modest contribution to the measured abundances.
- Considering MOS and pn spectra of each region individually in the fitting leads to 5−6% systematics in the whole 2.5−4.5 keV temperature range (Fig. 3, top).
- A joint fit of the MOS and pn spectra of each region leads on average to a 1−2% excess in the estimate of the systematics, with respect to the individual fits (Fig. 3, bottom).
- The systematics show no evident dependence on the X-ray flux (Fig. 4).

Finally, and especially when averaging iron abundances over a sufficiently large sample of clusters with temperatures lower than ∼3.5 keV, we suggest taking into account the measured 5−8% systematic contribution related to the L-shell to the derived abundances in order to correct L-shell-induced systematics.

Acknowledgements. We thank the anonymous referee for useful suggestions. G.R. acknowledges funding from Istituto Nazionale di Astrofisica (INAF) and from the AHEAD project (grant agreement n. 654215), which is part of the EU-H2020 programme. We acknowledge financial support contributions from contract n. 4000116655/16/NL/BW by ESA and from contract ASI-INAF n. 2019-27-HH.0. The results reported in this article are based on data obtained from the *XMM-Newton* observatory, an ESA science mission with instruments and contributions directly funded by ESA Member States and USA (NASA).

References

Arnaud, K. A. 1996, in Astronomical Data Analysis Software and Systems V, eds. G. H. Jacoby, & J. Barnes, ASP Conf. Ser., 101, 17

Asplund, M., Grevesse, N., Sauval, A. J., & Scott, P. 2009, ARA&A, 47, 481
Barret, D., den Herder, J. W., Piro, L., et al. 2013, ArXiv e-prints [arXiv:1308.6784]
Burbidge, E. M., Burbidge, G. R., Fowler, W. A., & Hoyle, F. 1957, Rev. Mod. Phys., 29, 547
Cameron, A. G. W. 1957, PASP, 69, 201
Cucchetti, E., Clerc, N., Pointecouteau, E., Peille, P., & Pajot, F. 2019, A&A, 629, A144
de Plaa, J., Werner, N., Bleeker, J. A. M., et al. 2007, A&A, 465, 345
Ebeling, H., Mullis, C. R., & Tully, R. B. 2002, ApJ, 580, 774
Eckert, D., Ettori, S., Pointecouteau, E., et al. 2017, Astron. Nachr., 338, 293
Farage, C. L., McGregor, P. J., & Dopita, M. A. 2012, ApJ, 747, 28
Foster, A. R., Ji, L., Smith, R. K., & Brickhouse, N. S. 2012, ApJ, 756, 128
Gastaldello, F., & Molendi, S. 2002, ApJ, 572, 160
Gastaldello, F., Simionescu, A., Mernier, F., et al. 2021, Universe, 7, 208
Gendron-Marsolais, M. L., Hlavacek-Larrondo, J., Clarke, T. E., et al. 2016, AAS/High Energy Astrophys. Div., 15, 101.03
Ghizzardi, S., De Grandi, S., & Molendi, S. 2014, A&A, 570, A117
Ghizzardi, S., Molendi, S., van der Burg, R., et al. 2021a, A&A, 646, A92
Ghizzardi, S., Molendi, S., van der Burg, R., et al. 2021b, A&A, 652, C3
Giacintucci, S., Markevitch, M., Cassano, R., et al. 2019, ApJ, 880, 70
Gu, L., Raassen, A. J. J., Mao, J., et al. 2019, A&A, 627, A51
Gu, L., Shah, C., Mao, J., et al. 2020, A&A, 641, A93
Guainazzi, M., & Tashiro, M. S. 2018, ArXiv e-prints [arXiv:1807.06903]
Heuer, K., Foster, A. R., & Smith, R. 2021, ApJ, 908, 3
Hitomi Collaboration (Aharonian, F., et al.) 2018, PASJ, 70, 12
Hwang, U., Mushotzky, R. F., Loewenstein, M., et al. 1997, ApJ, 476, 560
Kaastra, J. S., Mewe, R., & Nieuwenhuijzen, H. 1996, UV and X-ray Spectroscopy of Astrophysical and Laboratory Plasmas, 411
Kaastra, J. S., Raassen, A. J. J., de Plaa, J., & Gu, L. 2018, https://doi.org/10.5281/zenodo.2419563
Leccardi, A., & Molendi, S. 2008a, A&A, 487, 461
Leccardi, A., & Molendi, S. 2008b, A&A, 486, 359
Lovisari, L., & Reiprich, T. H. 2019, MNRAS, 483, 540
Mazzotta, P., Mazzitelli, G., Colafrancesco, S., & Vittorio, N. 1998, A&AS, 133, 403
Mernier, F., de Plaa, J., Kaastra, J. S., et al. 2017, A&A, 603, A80
Mernier, F., Biffi, V., Yamaguchi, H., et al. 2018, Space Sci. Rev., 214, 129
Molendi, S., Eckert, D., De Grandi, S., et al. 2016, A&A, 586, A32
Nomoto, K., Kobayashi, C., & Tominaga, N. 2013, ARA&A, 51, 457
Planck Collaboration XXIX. 2014, A&A, 571, A29
Planck Collaboration XXVII. 2016, A&A, 594, A27
Read, A. M., Guainazzi, M., & Sembay, S. 2014, A&A, 564, A75
Sanders, J. S., Fabian, A. C., & Smith, R. K. 2011, MNRAS, 410, 1797
Smith, R. K., Brickhouse, N. S., Liedahl, D. A., & Raymond, J. C. 2001, ApJ, 556, L91
Sun, M., Voit, G. M., Donahue, M., et al. 2009, ApJ, 693, 1142
Sunyaev, R. A., & Zeldovich, Y. B. 1972, Comments Astrophys. Space Phys., 4, 173
Tashiro, M., Maejima, H., & Toda, K. 2018, in Space Telescopes and Instrumentation 2018: Ultraviolet to Gamma Ray, eds. J. W. A. den Herder, S. Nikzad, & K. Nakazawa, SPIE Conf. Ser., 10699, 1069922
Walker, S., Simionescu, A., Nagai, D., et al. 2019, Space Sci. Rev., 215, 7
Werner, N., Sun, M., Bagchi, J., et al. 2011, MNRAS, 415, 3369

Appendix A: Iron-abundance measurements

In Table A.1 and Table A.2 we report the derived iron abundances for Perseus, 2A 0335+096, and Sérsic 159-03, measured after the exclusion of the L-shell ($Z_{K\alpha}$) and the Kα ($Z_{\text{L-shell}}$) and obtained either through the individual (Table A.1) or the joint (Table A.2) fit of MOS and pn spectra.

Table A.1. Iron abundance values measured for Perseus, 2A 0335+096, and Sérsic 159-03 after the exclusion of the L-shell ($Z_{K\alpha}$) and the Kα ($Z_{\text{L-shell}}$) and by individually fitting MOS and pn spectra of each region.

Cluster	Strategy	Rings (′)	$Z_{K\alpha}$ ($Z_\odot$)			$Z_{\text{L-shell}}$ ($Z_\odot$)		
			MOS 1	MOS 2	pn	MOS 1	MOS 2	pn
Perseus	1	0.5 – 1	0.695 ± 0.012	0.636 ± 0.011	0.582 ± 0.009	0.714 ± 0.010	0.683 ± 0.021	0.683 ± 0.008
		1 – 2	0.723 ± 0.009	0.659 ± 0.008	0.650 ± 0.006	0.758 ± 0.008	0.710 ± 0.014	0.691 ± 0.006
		2 – 3	0.697 ± 0.010	0.662 ± 0.009	0.630 ± 0.007	0.763 ± 0.011	0.652 ± 0.016	0.654 ± 0.007
	2	0.5 – 1	0.698 ± 0.012	0.655 ± 0.012	0.590 ± 0.010	0.713 ± 0.010	0.695 ± 0.010	0.654 ± 0.011
		1 – 2	0.744 ± 0.010	0.680 ± 0.008	0.661 ± 0.007	0.750 ± 0.007	0.718 ± 0.008	0.704 ± 0.006
		2 – 3	0.719 ± 0.010	0.664 ± 0.009	0.629 ± 0.007	0.757 ± 0.008	0.679 ± 0.012	0.672 ± 0.007
2A 0335+096	1	0.5 – 1	0.706 ± 0.027	0.701 ± 0.027	0.726 ± 0.019	0.676 ± 0.016	0.680 ± 0.018	0.763 ± 0.030
		1 – 2	0.628 ± 0.023	0.649 ± 0.022	0.632 ± 0.015	0.668 ± 0.027	0.699 ± 0.029	0.638 ± 0.027
		2 – 3	0.573 ± 0.058	0.536 ± 0.026	0.566 ± 0.019	0.675 ± 0.038	0.612 ± 0.036	0.623 ± 0.018
		3 – 4	0.453 ± 0.038	0.572 ± 0.035	0.520 ± 0.025	0.520 ± 0.029	0.575 ± 0.045	0.549 ± 0.025
		4 – 5	0.573 ± 0.049	0.498 ± 0.044	0.443 ± 0.029	0.547 ± 0.049	0.509 ± 0.055	0.546 ± 0.032
	2	0.5 – 1	0.706 ± 0.027	0.696 ± 0.026	0.728 ± 0.019	0.677 ± 0.022	0.680 ± 0.017	0.745 ± 0.011
		1 – 2	0.628 ± 0.023	0.645 ± 0.022	0.632 ± 0.015	0.660 ± 0.021	0.689 ± 0.021	0.668 ± 0.011
		2 – 3	0.544 ± 0.028	0.536 ± 0.026	0.568 ± 0.021	0.618 ± 0.026	0.593 ± 0.023	0.604 ± 0.017
		3 – 4	0.453 ± 0.034	0.572 ± 0.035	0.525 ± 0.025	0.507 ± 0.032	0.569 ± 0.034	0.539 ± 0.025
		4 – 5	0.569 ± 0.050	0.498 ± 0.045	0.448 ± 0.032	0.543 ± 0.042	0.507 ± 0.038	0.527 ± 0.029
Sérsic 159-03	1	0.5 – 1	0.452 ± 0.038	0.433 ± 0.031	0.403 ± 0.025	0.433 ± 0.024	0.480 ± 0.023	0.415 ± 0.012
		1 – 2	0.331 ± 0.030	0.337 ± 0.032	0.365 ± 0.021	0.332 ± 0.025	0.365 ± 0.019	0.343 ± 0.014
		2 – 3	0.273 ± 0.043	0.266 ± 0.040	0.308 ± 0.035	0.249 ± 0.023	0.333 ± 0.043	0.291 ± 0.022
	2	0.5 – 1	0.455 ± 0.033	0.429 ± 0.031	0.398 ± 0.021	0.433 ± 0.021	0.485 ± 0.024	0.429 ± 0.011
		1 – 2	0.332 ± 0.029	0.332 ± 0.028	0.352 ± 0.022	0.334 ± 0.021	0.367 ± 0.020	0.357 ± 0.011
		2 – 3	0.271 ± 0.042	0.267 ± 0.042	0.315 ± 0.036	0.255 ± 0.023	0.317 ± 0.025	0.297 ± 0.018

Table A.2. Same as Table A.1, but the MOS and pn spectra are jointly fitted.

Cluster	Rings (′)	Strategy 1		Strategy 2	
		$Z_{K\alpha}$ ($Z_\odot$)	$Z_{\text{L-shell}}$ ($Z_\odot$)	$Z_{K\alpha}$ ($Z_\odot$)	$Z_{\text{L-shell}}$ ($Z_\odot$)
Perseus	0.5 – 1	0.618 ± 0.006	0.677 ± 0.006	0.620 ± 0.006	0.672 ± 0.005
	1 – 2	0.669 ± 0.004	0.723 ± 0.004	0.677 ± 0.004	0.719 ± 0.004
	2 – 3	0.643 ± 0.005	0.686 ± 0.008	0.663 ± 0.005	0.692 ± 0.006
2A 0335+096	0.5 – 1	0.713 ± 0.013	0.731 ± 0.008	0.711 ± 0.014	0.738 ± 0.006
	1 – 2	0.628 ± 0.012	0.675 ± 0.008	0.628 ± 0.011	0.663 ± 0.008
	2 – 3	0.548 ± 0.015	0.633 ± 0.013	0.552 ± 0.013	0.591 ± 0.012
	3 – 4	0.511 ± 0.018	0.545 ± 0.017	0.512 ± 0.017	0.536 ± 0.016
	4 – 5	0.485 ± 0.024	0.554 ± 0.026	0.488 ± 0.023	0.523 ± 0.021
Sérsic 159-03	0.5 – 1	0.423 ± 0.016	0.440 ± 0.010	0.421 ± 0.015	0.445 ± 0.007
	1 – 2	0.338 ± 0.016	0.357 ± 0.008	0.341 ± 0.014	0.357 ± 0.008
	2 – 3	0.285 ± 0.022	0.286 ± 0.015	0.288 ± 0.024	0.287 ± 0.013

Appendix B: Perseus and Sérsic 159-03

In Fig. B.1 and Fig. B.2 we show the derived $\Delta Z/Z$ as a function of the cluster radius for Perseus and Sérsic 159-03, respectively. The $\Delta Z/Z$ values are obtained either by individually fitting each detector spectrum and from a joint fit.

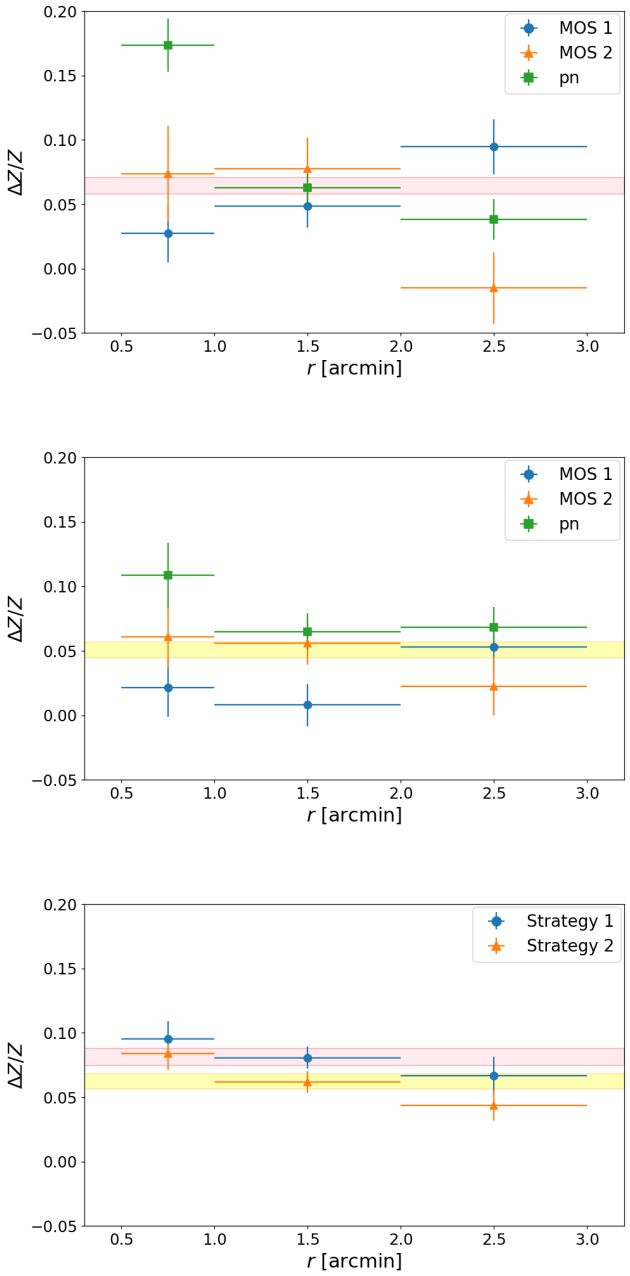

Fig. B.1. Radial profile of the systematic error $\Delta Z/Z$ for Perseus. In the top and centre panels the results obtained through an individual fit of the MOS and pn spectra of each region are shown, following strategy 1 and 2, respectively. In the bottom panel the same profiles are shown for the MOS and pn spectra that are considered jointly in the fitting. The weighted averages of the results are shown, together with their 1σ errors, as the pink and the yellow regions, for strategy 1 and 2, respectively.

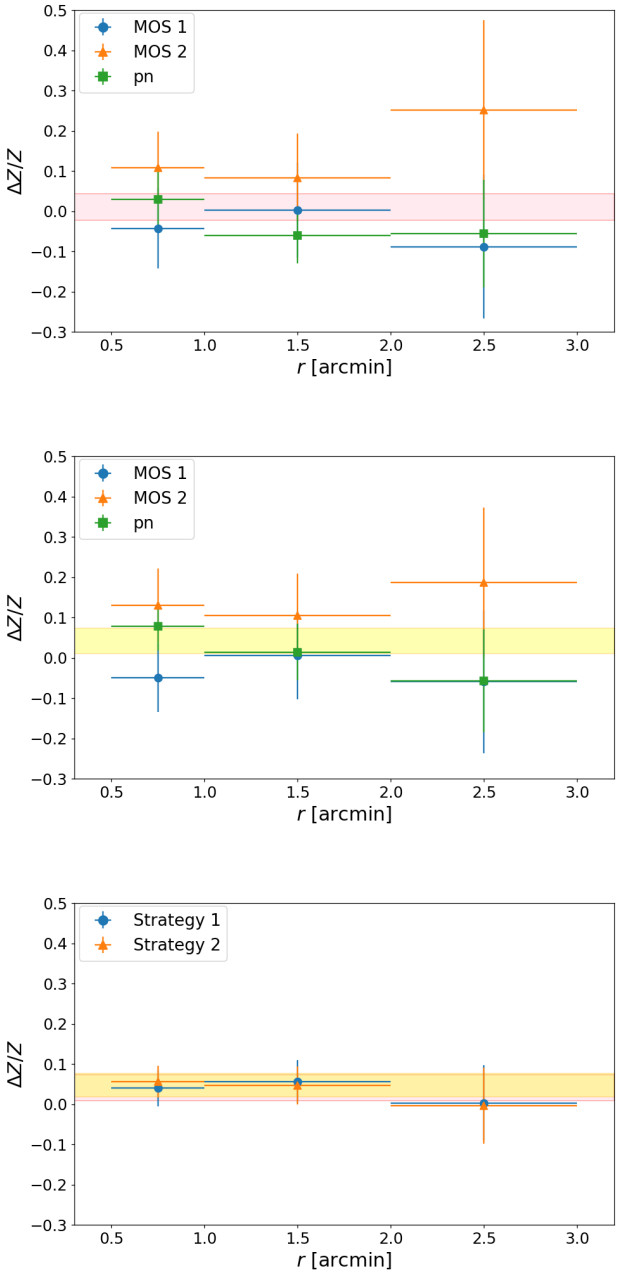

Fig. B.2. Same as Fig. B.1, but for Sérsic 159-03.

Appendix C: Temperature values

In Table C.1 we report the measured temperatures for Perseus, 2A 0335+096, and Sérsic 159-03, by individually fitting the MOS and pn spectra of each region, which is a useful sanity check. For spectra that were better described by the double-temperature model (see Sect. 3.2.2) we report a weighted-averaged temperature on the normalisations of the APEC+APEC model, calculated as

$$T = \frac{T_{\rm cold} \times {\rm norm}_{\rm cold} + T_{\rm hot} \times {\rm norm}_{\rm hot}}{{\rm norm}_{\rm cold} + {\rm norm}_{\rm hot}}, \quad \text{(C.1)}$$

where $T_{\rm cold}$ and $T_{\rm hot}$ are the lowest and the highest derived temperatures through the 2T model, while ${\rm norm}_{\rm cold}$ and ${\rm norm}_{\rm hot}$ are their respective normalisations.

Table C.1. Temperature values measured for Perseus, 2A 0335+096, and Sérsic 159-03 by individually fitting MOS and pn spectra of each region.

Cluster	Rings (′)	Temperature (keV)		
		MOS 1	MOS 2	pn
Perseus	0.5 – 1	3.924 ± 0.087	3.933 ± 0.119	3.696 ± 0.055
	1 – 2	4.369 ± 0.088	4.161 ± 0.073	4.042 ± 0.036
	2 – 3	5.212 ± 0.165	4.900 ± 0.226	4.671 ± 0.072
2A 0335+096	0.5 – 1	2.565 ± 0.124	2.539 ± 0.156	2.431 ± 0.047
	1 – 2	3.248 ± 0.288	3.266 ± 0.428	3.039 ± 0.138
	2 – 3	3.326 ± 0.024	3.230 ± 0.033	3.198 ± 0.020
	3 – 4	3.430 ± 0.055	3.439 ± 0.042	3.347 ± 0.023
	4 – 5	3.493 ± 0.078	3.390 ± 0.068	3.357 ± 0.052
Sérsic 159-03	0.5 – 1	2.750 ± 0.353	2.532 ± 0.103	2.688 ± 0.187
	1 – 2	2.768 ± 0.414	2.666 ± 0.213	2.729 ± 0.345
	2 – 3	2.564 ± 0.034	2.536 ± 0.039	2.585 ± 0.028

Notes. For cluster rings that were better described by the 2T model, we report a weighted-averaged temperature on the normalisations of the APEC+APEC model (see text for details).